Topological metals induced by the Zeeman effect

Song Sun,[1,2] Zhida Song,[1,2] Hongming Weng,[1,2,3] and Xi Dai[4,*]

[1]*Beijing National Laboratory for Condensed Matter Physics, and Institute of Physics, Chinese Academy of Sciences, Beijing 100190, China*

[2]*University of Chinese Academy of Sciences, Beijing 100049, China*

[3]*Collaborative Innovation Center of Quantum Matter, Beijing 100084, China*

[4]*Department of Physics, Hong Kong University of Science and Technology, Clear Water Bay, Kowloon 999077, Hong Kong*

(Received 20 October 2019; revised manuscript received 16 January 2020; accepted 27 February 2020; published 19 March 2020)

In this paper, we propose a new topological classification for Zeeman split Fermi surfaces of centrosymmetric metals under external magnetic field, where the Zeeman effect is described by the momentum-dependent g-factor tensor. With three important experimental effects, modification of spin-zero effect, Zeeman-effect-induced Fermi surface Chern number, and the in-plane anomalous Hall effect, we reveal that the additional Zeeman-induced Berry curvature plays a crucial role in the electron dynamics for metals under magnetic field, which has been overlooked for decades. By first-principles calculations, we study all these effects on two typical material, $ZrTe_5$ and $TaAs_2$ and the results are in good agreement with the existing experiments.

DOI: 10.1103/PhysRevB.101.125118

I. INTRODUCTION

How a condensed matter system responds to an external magnetic field is one of the key properties signaling its low-energy electronic structure. For metallic systems, most of the magnetic responses, such as quantum oscillation spectrum, magnetoresistance, and Hall effects, are determined by the Bloch states at the Fermi surfaces (FSs) only, where in nonmagnetic centrosymmetric metals the effects caused by the magnetic field can be ascribed to two parts, the Zeeman effect that splits the otherwise degenerate bands and the orbital effect that leads to Landau levels. Without magnetic field, due to the time-reversal and inversion symmetries, the Fermi surfaces always have twofold degeneracy and the Berry curvature in this case is SU(2) and traceless. Once a magnetic field is applied, the Zeeman effect described by a momentum dependent 2×2 g-factor tensor will split the doubly degenerate FS into two separate ones, with each one of them being treated as a nondegenerate system carrying ordinary U(1) Berry curvature, which is crucial to determine the low-energy dynamics of the Bloch electrons around the FS. Most importantly, the Zeeman-effect-induced U(1) Berry curvature can be very large in metals with large spin orbital coupling under specific external magnetic direction and leads to several interesting physical phenomena, which have been overlooked for decades.

In general, for such systems the Zeeman effect is described by the g-factor tensor, which can be expressed as a momentum-dependent vector valued 2×2 matrix $\hat{\boldsymbol{g}}(\boldsymbol{k})$. As discussed in detail previously [1–3], the renormalization of the g-factor tensor from its vacuum value as well as its momentum dependence are both caused by the high-energy bands through the down-folding process, or equivalently due to the effective screening process for the diamagnetic current. After down-folding to the lowest bands forming the FS, the Zeeman-effect-induced Berry connection can be fully determined by the g-factor tensor $\hat{\boldsymbol{g}}(\boldsymbol{k})$ and the original SU(2) non-Abelian Berry connection $\hat{\boldsymbol{\mathcal{A}}}(\boldsymbol{k})$ on the FS.

Such Zeeman-effect-induced Berry connection can lead to many interesting physical phenomena. First of all, the induced additional Berry connection will contribute a phase to the quantization condition for Landau orbits, which can be detected directly by the quantum oscillation spectrum [4–6]. As will be introduced below, such additional phase will strongly modify the spin-zero effect [7] in these materials, in which the amplitude of quantum oscillation will vanish completely at some special angles determined by the Zeeman effect. In traditional materials, the spin-zero angles are fully determined by the splitting of the areas enclosed by Landau orbits for two different spin [7]. While, for metals with strong spin orbital coupling these spin-zero angles acquired considerable contributions from Zeeman-induced Berry phases accumulated on two different Landau orbits, which will greatly change the spin-zero angles. Second, the Zeeman-induced Berry curvature will contribute to the Hall effect in addition to the ordinary Lorentz force, which has the same origin with the anomalous Hall effect [8–10] in the ferromagnetic metals. When the magnetic field is applied within the plane of current and voltage, the Lorentz force can be neglected and such an in-plane anomalous Hall effect is mainly contributed by the Zeeman-effect-induced Berry curvature and can be quite pronounced in some materials as shown below. This nonzero in-plane anomalous Hall effect is counterintuitive and only can be calculated with this momentum-dependent g-factor tensor for metals with nonconcentrated FS. Last, most interestingly, such Zeeman-induced Berry curvature can be integrated over each particular closed FS and leads to topological metal phase [11–20] under the magnetic field if such integrations reach nonzero integers. In such cases, these

*daix@ust.hk

otherwise degenerate FS will split into two with opposite nonzero Chern numbers, which will lead to similar chiral magnetic effect [21–23] and negative magnetoresistance [24–26] as those Weyl semimetals. Here we want to emphasize that, different from previous work [3,13,27] where the Zeeman effect is only considered for Dirac or Weyl semimetals and the absolute and momentum-independent (constant) g-factor is sufficient to induce topological phase transition, in the present paper we focus on the topological trivial metal with ordinary doubly degenerate FS, where the Zeeman-induced Berry curvature and Chern numbers are purely caused by the topological structure of the g-factor tensor over the manifold of the FS.

In the present paper, we will first introduce the general theory for the Zeeman-induced Berry curvature in nonmagnetic centrosymmetric metals. After that, we will take $ZrTe_5$ and $TaAs_2$ as two typical examples to introduce the spin-zero effect, in-plane anomalous Hall effect and the field-induced topological metals in these material systems.

II. THEORY

In nonmagnetic centrosymmetric systems, the Bloch states are always doubly degenerate at any $\boldsymbol{k}$ point, which is guaranteed by the combination of time-reversal and space-inversion symmetry $\mathcal{PT}$. There is a SU(2) gauge freedom stemming from the degenerate subspace at each $\boldsymbol{k}$ point, and the non-Abelian traceless Berry connection $\hat{\boldsymbol{\mathcal{A}}}_{aa'}(\boldsymbol{k}) = i\langle\psi_a|\partial_{\boldsymbol{k}}\psi_{a'}\rangle$ and Berry curvature $\hat{\boldsymbol{\mathcal{F}}}(\boldsymbol{k}) = \nabla_{\boldsymbol{k}} \times \hat{\boldsymbol{\mathcal{A}}} - i\hat{\boldsymbol{\mathcal{A}}} \times \hat{\boldsymbol{\mathcal{A}}}$ can be defined, which determines the low-energy dynamics for the quasiparticles near the Fermi level. Here $|\psi_a\rangle$ represents bases of the degenerate subspace. Under a U(2) gauge transformation $\hat{U}(\boldsymbol{k})$, the above Berry connection and curvature are transformed in the following way [28]: $\hat{\boldsymbol{\mathcal{A}}}' = \hat{U}^\dagger\hat{\boldsymbol{\mathcal{A}}}\hat{U} + i\hat{U}^\dagger\partial_{\boldsymbol{k}}\hat{U}$, $\hat{\boldsymbol{\mathcal{F}}}' = U^\dagger\hat{\boldsymbol{\mathcal{F}}}U$. When magnetic field is applied, the Zeeman's coupling $\hat{H}^z_{aa'} = \mu_B\hat{\boldsymbol{g}}_{aa'}(\boldsymbol{k})\cdot\boldsymbol{B}$ will break the time-reversal symmetry and split the degenerate states. In this case, the Berry connection reduces to U(1) and can be obtained from the previous SU(2) Berry connection $\hat{\boldsymbol{\mathcal{A}}}(\boldsymbol{k})$ and a specific SU(2) matrix $\hat{U}(\boldsymbol{k})$, which diagonalize the Zeeman's coupling at each particular $\boldsymbol{k}$ point as $\boldsymbol{A}_\pm = \pm\frac{1}{2}\mathrm{Tr}[\hat{U}^\dagger\hat{\boldsymbol{\mathcal{A}}}\hat{U}\hat{\sigma}_z + i\hat{U}^\dagger\partial_{\boldsymbol{k}}\hat{U}\hat{\sigma}_z]$ with the $\pm$ sign representing the two branches of bands after splitting and $\hat{\sigma}_z$ representing the third Pauli matrix. Since the original SU(2) Berry connection $\hat{\boldsymbol{\mathcal{A}}}(\boldsymbol{k})$ is traceless, we always have $\boldsymbol{A}_+ = -\boldsymbol{A}_-$. Details about the properties of SU(2) Berry connection under $\mathcal{PT}$ symmetry are given in Appendix A. It is worth emphasizing that the U(1) Berry connection $\boldsymbol{A}_\pm(\boldsymbol{k})$ is determined not only by the topological features of the degenerate band structure before the Zeeman splitting, the SU(2) Berry connection $\hat{\boldsymbol{\mathcal{A}}}(\boldsymbol{k})$, but also by the topological structure hidden in the momentum-dependent g-factor $\hat{\boldsymbol{g}}(\boldsymbol{k})$. Therefore, to determine the topological features of a metallic system with Zeeman split FS, the dependence of the g-factor on the FS is essential.

In our previous paper [3], we have already developed the computational method to compute the momentum-dependent g factor, which will be briefly sketched here. In solid-state systems, not only the spin but also the orbital responses contribute to the g factor. The spin contribution $\hat{\boldsymbol{g}}^s$ can be calculated directly from the corresponding Bloch eigenstates $\hat{\boldsymbol{g}}^s_{mm'} = \frac{2}{\hbar}\langle\psi_{\boldsymbol{K}m}|\hat{\boldsymbol{s}}|\psi_{\boldsymbol{K}m'}\rangle$,where $\hat{\boldsymbol{s}}$ is the spin operator. The orbit contribution caused by the high-energy bands through the down-folding process is introduced as follows. Around the wave vector $\boldsymbol{K}$, the bare $\boldsymbol{k}\cdot\boldsymbol{p}$ Hamiltonian has the form [29]

$$\hat{H}_{nn'} = \delta_{nn'}\left(\epsilon_n + \frac{\hbar^2\boldsymbol{k}^2}{2m_e}\right) + \hat{\boldsymbol{v}}_{nn'}\cdot\boldsymbol{k}. \tag{1}$$

Here ϵ_n is the band energy at $\boldsymbol{K}$, and m_e is the electron rest mass in vacuum. At the wave vector $\boldsymbol{k}+\boldsymbol{K}$, the term $\hat{\boldsymbol{v}}_{nn'}\cdot\boldsymbol{k}$ result in the mixing of the eigenstates $|\psi_{\boldsymbol{K}n}\rangle$ and $\hat{\boldsymbol{v}}_{nn'}$ depends on $\boldsymbol{K}$. An unitary transformation can be obtained by the quasidegenerate perturbation to decouple the subspace we focus on (called low-energy subspace) from all the other bands (called high-energy subspace) [29,30]

$$\hat{H}_{mm'} = \delta_{mm'}\left(\epsilon_m + \frac{\hbar^2\boldsymbol{k}^2}{2m_e}\right) + \hat{\boldsymbol{v}}_{mm'}\cdot\boldsymbol{k} + \frac{1}{2}\sum_{l,ij}\left(\frac{1}{\epsilon_m-\epsilon_l} + \frac{1}{\epsilon_{m'}-\epsilon_l}\right)\hat{v}^i_{ml}\hat{v}^j_{lm'}k^ik^j, \tag{2}$$

where the index m, m' are the band indexes for the low-energy subspace, and l is the band index for the high-energy subspace. In the presence of magnetic field, according to Peierls substitution the momenta k^i should be replaced by the canonical momentum operators $k^i \to (-i\partial^i + \frac{e}{\hbar}A^i)$, where A^i is the vector potential. Hence $k^ik^j \to (-i\partial^i + \frac{e}{\hbar}A^i)(-i\partial^j + \frac{e}{\hbar}A^j)$, which can be decomposed into a symmetric component with gauge-dependent explicit form $\frac{1}{2}\{-i\partial^i + \frac{e}{\hbar}A^i, -i\partial^j + \frac{e}{\hbar}A^j\}$ and an antisymmetric component with gauge-independent explicit form $\frac{1}{2}[-i\partial^i + \frac{e}{\hbar}A^i, -i\partial^j + \frac{e}{\hbar}A^j] = -\frac{ie}{2\hbar}\sum_k\varepsilon_{ijk}B_k$, which contributes to orbital Zeeman's coupling. In summary, under magnetic field the total Hamiltonian consists of two parts: a gauge-dependent explicit form part, which leads to Landau level $H^L_{mm'}$ and a gauge-invariant explicit form part, which is the Zeeman's coupling $H^Z_{mm'}$, which can be written as,

$$\hat{H}^L_{mm'} = \delta_{mm'}\epsilon_m + \hat{\boldsymbol{v}}_{mm'}\cdot\left(-i\nabla + \frac{e}{\hbar}\boldsymbol{A}\right) + \sum_{ij}\hat{M}^{ij}_{mm'}\left(-i\partial^i + \frac{e}{\hbar}A^i\right)\left(-i\partial^j + \frac{e}{\hbar}A^j\right) \tag{3}$$

$$\hat{H}^Z_{mm'} = \mu_B\left(\hat{\boldsymbol{g}}^o_{mm'} + \hat{\boldsymbol{g}}^s_{mm'}\right)\cdot\boldsymbol{B}, \tag{4}$$

where

$$\hat{M}^{ij}_{mm'} = \delta_{mm'}\delta_{ij}\frac{\hbar^2}{2m_e} + \frac{1}{4}\sum_l\left(\frac{1}{\epsilon_m-\epsilon_l} + \frac{1}{\epsilon_{m'}-\epsilon_l}\right)\times\left(\hat{v}^i_{ml}\hat{v}^j_{lm'} + \hat{v}^j_{ml}\hat{v}^i_{lm'}\right) \tag{5}$$

$$\hat{\boldsymbol{g}}^o_{mm'} = -\frac{im_e}{2\hbar^2}\sum_{l,ijk}\left(\frac{1}{\epsilon_m-\epsilon_l} + \frac{1}{\epsilon_{m'}-\epsilon_l}\right)\hat{v}^i_{ml}\hat{v}^j_{lm'}\varepsilon_{ijk}\boldsymbol{e}_k. \tag{6}$$

Here $\boldsymbol{e}_k$ is the unit direction vector and μ_B is the Bohr magneton. Please note that only in this paragraph by saying the g-factor tensor is momentum-dependent we mean the g-factor tensor depends on $\boldsymbol{K}$ not $\boldsymbol{k}$.

III. VANISHING QUANTUM OSCILLATIONS

The first observable that manifests the momentum and field direction dependence of the Zeeman's coupling is the spin-zero effect [7], where the Shubnikov-de Haas oscillation (SdH) or de Haas-Von Alphen (dHV) effect vanishes when the field is applied along some special directions. The SdH or dHV effect is the oscillation of the resistance or magnetic susceptibility that occurs under magnetic field. According to the Lifshitz-Kosevich formula, in the semiclassical limit the oscillations contributed by one FS are expressed as $\Delta\rho(B) \propto \cos(\hbar S_{\rm ex}/eB + \gamma + \phi)$, where $S_{\rm ex}$ is the area of the extreme cross section of the FS, which is perpendicular to the magnetic field (Refs. [7,31] have detailed explanation about the extreme cross section and Lifshitz-Kosevich formula), ϕ is the Berry phase over the boundary of the extreme cross section $\partial S_{\rm ex}$, the extra phase γ equals $-\pi/4$ or $\pi/4$ for maximum or minimum extreme cross section, respectively, and the sum is over the different extreme cross-section area. A striking effect, called spin-zero effect, manifests itself as the vanishing of quantum oscillations at some certain field directions, could happen when the doubly degenerate FS split into two under the Zeeman effect and thus contribute two oscillation terms with slightly different frequency and phases. More specifically, the Zeeman effect described by the g-factor tensor $\hat{\boldsymbol{g}}(\boldsymbol{k})$ leads to not only the splitting of the cross-section area $S_{\rm ex} = S^0_{\rm ex} \pm \alpha B$ but also an extra splitting U(1) Berry phase $\pm\phi$ as we introduced above. Here the $S_{\rm ex}$ ($S^0_{\rm ex}$) represents the cross-section area with (without) magnetic field. Hence, by applying the sum-to-product identity, the total oscillations of the two splitting FS are expressed as

$$\Delta\rho(B) \propto \cos\left(\frac{\hbar S^0_{\rm ex}}{eB} + \gamma\right)\cos\left(\frac{\hbar\alpha}{e} + \phi\right), \tag{7}$$

where

$$\alpha = \oint_{\partial S^0_{\rm ex}} \frac{\sqrt{|\det[\mu_B \hat{\boldsymbol{g}}(\boldsymbol{k})\cdot\boldsymbol{e}_B]|}}{\chi|\nabla_{\boldsymbol{k}}\epsilon(\boldsymbol{k})\times\boldsymbol{e}_B|}dk \tag{8}$$

$$\phi = \oint_{\partial S^0_{\rm ex}} \boldsymbol{A}_+(\boldsymbol{k})\cdot d\boldsymbol{k}. \tag{9}$$

Here $\chi = -1$ for electronlike valley, $\chi = 1$ for holelike valley, $\epsilon(\boldsymbol{k})$ is the band energy of FS states at $\boldsymbol{k}$, ϕ is the Berry phase accumulated along one of the split FS's extreme area and $\boldsymbol{e}_B$ is the direction of the magnetic field. The last part of Eq. (7) $R_s = \cos(\frac{\hbar\alpha}{e} + \phi)$ is the amplitude of oscillations, which depends on the direction of magnetic field. The spin-zero effect would happen at certain field directions where R_s equals zero. We would emphasize that for materials with strong SOC in order to obtain the right field direction for the spin-zero effect one has to compute both the coefficient α (for the splitting of FS area) and ϕ [for the splitting of U(1) Berry phase]. As shown in Eq. (8) and (9), both of them can be obtained from the momentum-dependent g-factor tensor on the FS (details are given in Appendix B).

The narrow gap semiconductor $ZrTe_5$, which only has small ellipsoid FS around the Γ point and shows strong anisotropy [32–35], is an ideal platform to study the spin-zero effect. With the parameters given in Ref. [3], we calculate the oscillation amplitude factor of the oscillation R_s for all the field directions as illustrated in Fig. 1, from which we can obtain the angles of spin zero, which are summarized and compared with experiments [36] in Table I. The theoretical results are consistent with the experimental results only when the Berry phase contributions are included. If we only consider the splitting of FS area, the corresponding results cannot match the experimental data even qualitatively.

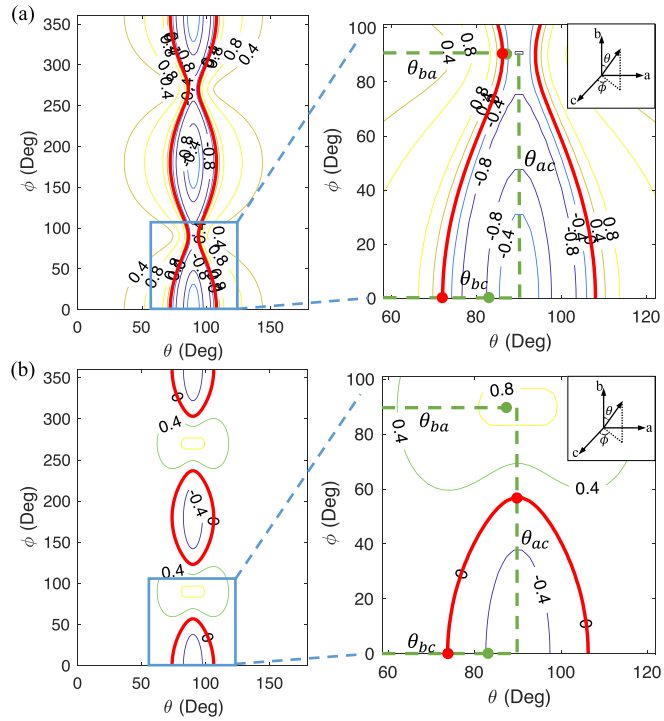

FIG. 1. Numerical calculations of the direction dependence of oscillation amplitudes factor $R_s(\boldsymbol{e}_B)$ based on GGA parameters given by Ref. [3] with Fermi energy $\mu_F = 0.026$ eV($\mu_F = 0$ eV is at the middle of the gap) in $ZrTe_5$. Oscillation amplitudes (a) with Berry phase contribution and (b) without Berry phase contribution are plotted individually. The angular for vanishing quantum oscillation are indicated by bold red line. The angles measured in Ref. [36] are indicated by green dotted line. We only keep linear approximation of $\boldsymbol{k}$ because of the tiny FS in ZrTe5. Inset is a schematic illustration of the geometry for axes. The FS is an ellipsoid with principal semiaxes $k_a = 0.118$ nm^{-1}, $k_b = 0.666$ nm^{-1}, and $k_c = 0.153$ nm^{-1}, which agrees well with the experiments [36].

IV. IN-PLANE HALL EFFECT AND FIELD-INDUCED TOPOLOGICAL METALS

In the presence of magnetic field, the Zeeman effect splits the degenerate states into $|\Psi_\pm(\boldsymbol{k})\rangle$ with splitting energy $\pm\Delta\epsilon^z$. The Chern numbers defined on each split Fermi surface

TABLE I. The angles of spin-zero effect

	Theory	Theory (no Berry phases)	Experiment [36]
θ_{bc}	72.0	73.7	83.8
θ_{ba}	86.1	∅	86.5
θ_{ac}	∅	56.8	∅

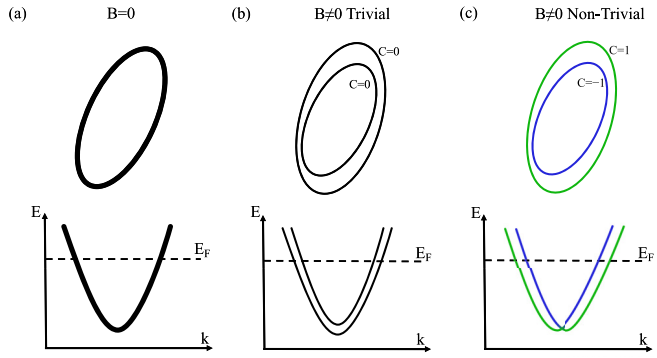

FIG. 2. Schematic diagrams for the mechanism of topological phase transition induced by the Zeemans coupling. The ellipses represent Fermi surfaces in a plane of momentum space. When there is no magnetic field, the $\mathcal{PT}$ symmetry make the states doubly degenerate indicated by bold curve in (a). In the presence of magnetic field, the Zeeman's coupling splits the degenerate states and Fermi surfaces split into two. For some directions of magnetic field, the Chern number of both Fermi surfaces are zero as shown in (b) and there is no Weyl point enclosed by the Fermi surfaces. For other directions of magnetic field, the Fermi surfaces have opposite nonzero Chern numbers as shown in (c) and there is a Weyl point enclosed by the Fermi surfaces. Here we only plot the most common and simple case.

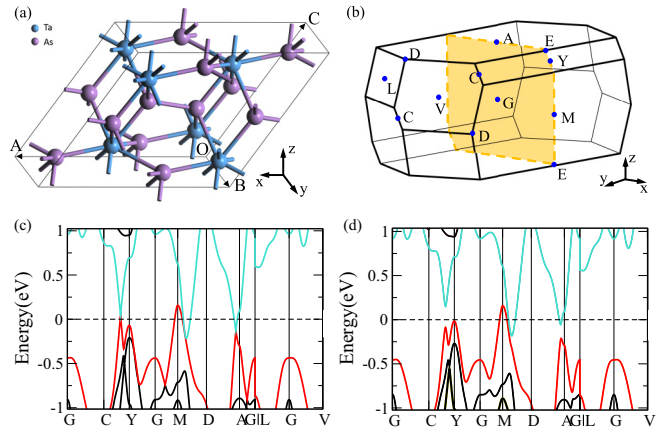

FIG. 3. Crystal structure, Brillouin zone and Band structure. (a) Crystal structure of $TaAs_2$ [42]. (b) The first Brillouin zone for $TaAs_2$. The yellow plane shows the position of mirror plane and high symmetry points is indicated by blue dot. (c), (d) Band structure for $TaAs_2$ (c) without SOC and (d) with SOC. From this we can find two electron-like pockets and one holelike pocket.

are well-defined topological invariances that characterize the topological nature of that particular metal under magnetic field, which can be expressed as

$$\mathcal{C}_{\pm} = \frac{1}{2\pi}\int_{FS} d\boldsymbol{S}\cdot\boldsymbol{F}_{\pm}(\boldsymbol{k}). \tag{10}$$

We can calculate the Chern numbers of all the Fermi surfaces with Willson loop method after including the Zeeman effect described by the g-factor tensor introduced previously. It is easy to prove that such FS Chern numbers will be only determined by the direction of the field and in general they can vary with the field direction, which defines the topological phase transition on the FS. A schematic plot of Zeeman-effect-induced nonzero Chern number on FS is shown in Fig. 2. Theoretically, classifications of topological metals with $\mathcal{PT}$ symmetry has been studied in Ref. [37]. Experimentally, the nonzero Chern numbers on FS will lead to similar chiral anomaly phenomena [24,26] and negative longitudinal magnetoresistance [38,39], which has been observed already in some of these materials [25,40].

Another way to manifest the Zeeman-effect-induced Berry phase and curvature on the FS is to look at the anomalous Hall effect, which is the Hall effect caused not by Lorentz force but the Zeeman-induced Berry curvature around the FS. In order to minimize the interference from the Lorentz force, which exists for generic setup, it is better to apply the field within the plane of the experimental setup for the Hall measurement. Generally, anomalous Hall coefficient (AHC) can be expressed by the integral of Berry curvature over the Brillouin zone [8,41] as

$$\sigma_{ij} = -\varepsilon_{ijk}\frac{e^2}{\hbar}\sum_n\int_{BZ}\frac{d^3\boldsymbol{k}}{(2\pi)^3}f(\epsilon_n(\boldsymbol{k}))F_n^k(\boldsymbol{k}). \tag{11}$$

Here, $F_n^k(\boldsymbol{k})$ represent the Berry curvature of the nth band in k direction at $\boldsymbol{k}$ wave vector and ε_{ijk} is the Levi-Civita notation. At zero magnetic field, the two degenerate states with opposite Berry curvature will be always both occupied or unoccupied and their contribution will cancel each other. With the presence of magnetic field, the Zeeman effect will split these states and the net contribution to the AHC comes from a thin shell near the FS where only one of these otherwise degenerate states is occupied. Using the momentum-dependent g-factor tensor introduced above, we can express the AHC as $\sigma_{ij} = \lambda_{ij,k}B_k$, where

$$\lambda_{ij,k} = -\varepsilon_{ijk}\frac{e^3}{m_e}\int_{FS}\frac{dS}{(2\pi)^3}\frac{\sqrt{|\det[\hat{\boldsymbol{g}}(\boldsymbol{k})\cdot\boldsymbol{e}_B]|}}{\chi|\nabla_{\boldsymbol{k}}\epsilon(\boldsymbol{k})|}F_+^k(\boldsymbol{k}). \tag{12}$$

Here, B is the strength of the magnetic field, $F_+^k(\boldsymbol{k})$ represents the Berry curvature of split state $|\Psi_+(\boldsymbol{k})\rangle$ and the definition of χ, $\boldsymbol{e}_B$ and $\epsilon(\boldsymbol{k})$ is same as Eq. (8). In particular, if the direction of magnetic field $\boldsymbol{e}_B$ is in the ij plane, we will get the in-plane AHC, in which the voltage, current, and magnetic field are all in the same plane.

In the present study, we take $TaAs_2$, an topological trivial semimetal with a number of tiny Fermi pockets, as a typical material example for the Zeeman-effect-induced FS Chern number and in-plane anomalous Hall effect. $TaAs_2$ crystallizes [42] in monoclinic structure with centrosymmetric space group of C2/m (No.12) as shown in Fig. 3(a). It has a binary axis (twofold rotation symmetry) along y direction and a mirror plane perpendicular to y direction. We performed the first-principles calculations by using the generalized gradient approximation (GGA) for the exchange-correlation functional with the Vienna *ab initio* simulation package (VASP). The cutoff energy for basis set is 400 eV and k-point sampling grid is $9\times9\times7$.

The calculated electronic structure of $TaAs_2$ are shown in Figs. 3(c), 3(d). Without SOC, the band structure of $TaAs_2$ contains a number of nodal lines, which is similar with TaAs. When the SOC is turned on, due to the

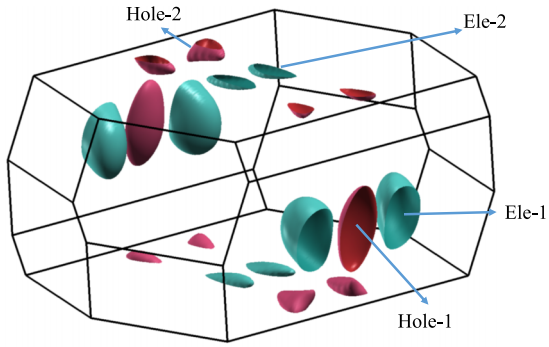

FIG. 4. Fermi surfaces in the first Brillouin zone. According to the symmetry, there are four nonequivalent Fermi surfaces in the first Brillouin zone. Two of them indicated in green are electronlike. The others indicated in red are holelike.

presence of inversion symmetry, a complete gap will be opened on all the line nodes and the band structure has been checked to be completely trivial in contrast to its cousin TaAs. Since the conduction and valence bands are still overlapping after including the SOC, $TaAs_2$ becomes a typical trivial semimetal with compensating electron and hole pockets. Around each pocket, the effective $\boldsymbol{k}\cdot\boldsymbol{p}$ models are 4×4 and can be generically described by a anisotropic Dirac equations with tiny mass terms (comparing to the chemical potential) leading to strong mixing between the conduction and valence bands near the band minimum (maximum), which is the microscopic origin for the strong momentum-dependent g-factor tensor. The Fermi surface plot in Fig. 4 clearly shows that totally there are nine FS in the first Brillouin zone, which can be divided into four nonequivalent types according to the crystal symmetries. From the first-principles results, we can construct the second-order $\boldsymbol{k}\cdot\boldsymbol{p}$ model Hamiltonian near the centers of each FS together with the k-dependent g-factor tensor, with which the FS chern numbers after the Zeeman splitting have been calculated and shown in Fig. 5 (details of our calculations are given in Appendix B). We find that indeed there are topological phase transitions in this material when we vary the direction of magnetic field. Please note that the zero Chern number of Hole-1 for all field directions is ensured by the inversion symmetry. For those FS with nonzero Chern numbers under the magnetic field, we have confirmed that there are Zeeman-effect-induced Weyl points enclosed within these FS. These Weyl points may contribute to negative magnetoresistance, which has already been found in $TaAs_2$ [43,44]

We also calculated the in-plane anomalous Hall coefficients of $TaAs_2$ in xy, yz, and zx planes. By considering the crystal symmetries, the only allowed in-plane anomalous Hall coefficients are $\lambda_{xy,x}$ and $\lambda_{yz,z}$, which are plotted in Fig. 6 as the function of chemical potential. We find that significant magnitude of in-plane anomalous Hall effect can be realized in $TaAs_2$. Interestingly, the sign of such in-plane anomalous Hall coefficient keeps unchanged even when the carrier type changes from n to p as the function of chemical potential, which is qualitatively different with the ordinary Hall effect caused by Lorentz force.

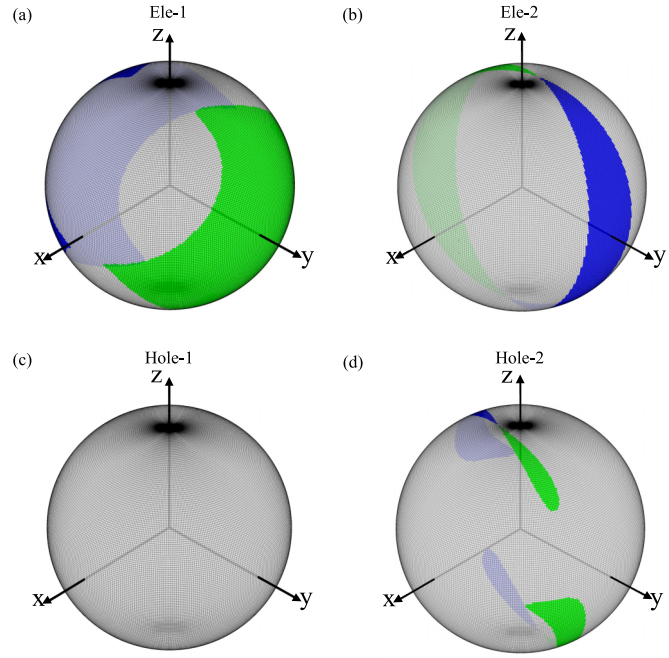

FIG. 5. The Chern number of four nonequivalent Fermi surfaces under different magnetic field directions. Directions of magnetic field are represented by points on the unit sphere. Chern number $=1$ is indicated in green and Chern number -1 is indicated in blue. Here we plot the Chern number of Fermi surface states $|\Psi_+(\boldsymbol{k})\rangle$. The other one $|\Psi_-(\boldsymbol{k})\rangle$ must have the opposite Chern number. They are in accordance with the symmetry possessed by the Fermi surface. As a result of inversion symmetry possessed by Hole-1, the Chern number is zero for all magnetic field directions shown in (c).

V. SUMMARY

In summary, we have proposed that the Zeeman effect caused by the external magnetic field can be in general described by momentum-dependent g-factor tensor, which can be also viewed as the effective low-energy Hamiltonian on

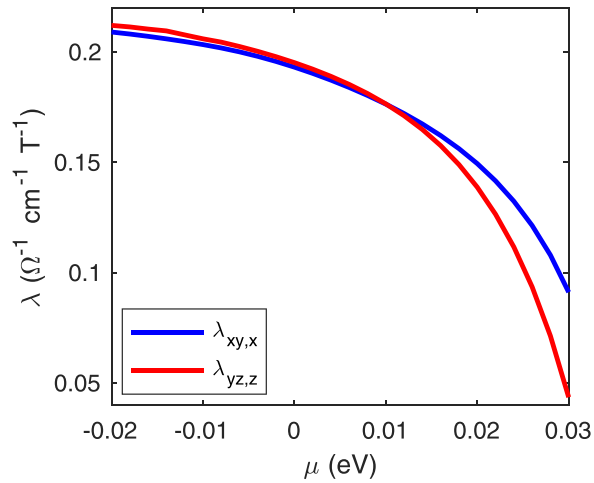

FIG. 6. In-plane anomolous Hall coefficient of $TaAs_2$ as the function of chemical potential. The In-plane anamolous Hall coefficient in xy plane $\lambda_{xy,x}$ is indicated in blue line and coefficient in yz plane $\lambda_{yz,z}$ is indicated in red line.

the FS of centrosymmetric metals. The topological features hidden in such g-factor tensor can manifest themselves by generating additional Zeeman-effect-induced Berry phase for Landau orbits, in-plane Hall effect, and even nonzero Chern numbers on Zeeman split FS. All these exotic effects are demonstrated on two of the typical materials, $ZrTe_5$ and $TaAs_2$, by means of first-principles calculations indicating that the effects proposed in the present study should widely exist in metals with inversion symmetry and strong SOC.

ACKNOWLEDGMENTS

We acknowledge the financial support from the Hong Kong Research Grants Council (Project No. GRF16300918), and thank Prof. Liyuan Zhang, Xiaosong Wu, and Haizhou Lu for invaluable discussions.

APPENDIX A: $\mathcal{PT}$ SYMMETRY

Generally for a nonmagnetic centrosymmetric crystal, the representation of operation $\mathcal{P}$ and $\mathcal{T}$ can be written as follows:

$$\mathcal{P}|\psi_1(\boldsymbol{k})\rangle = |\psi_2(-\boldsymbol{k})\rangle \qquad \mathcal{P}|\psi_2(\boldsymbol{k})\rangle = |\psi_1(-\boldsymbol{k})\rangle \tag{A1}$$

$$\mathcal{T}|\psi_1(\boldsymbol{k})\rangle = |\psi_2(-\boldsymbol{k})\rangle \qquad \mathcal{T}|\psi_2(\boldsymbol{k})\rangle = -|\psi_1(-\boldsymbol{k})\rangle. \tag{A2}$$

Hence for little group at any wave vector $\boldsymbol{k}$ there is at least one generator named $\mathcal{PT}$, and the representation is

$$\mathcal{PT}|\psi_1(\boldsymbol{k})\rangle = |\psi_2(\boldsymbol{k})\rangle \qquad \mathcal{PT}|\psi_2(\boldsymbol{k})\rangle = -|\psi_1(\boldsymbol{k})\rangle \tag{A3}$$

or equivalently in matrix form

$$D(\mathcal{PT}) = \begin{pmatrix} 0 & -1 \\ 1 & 0 \end{pmatrix}, \tag{A4}$$

where $\mathcal{PT}|\psi_i(\boldsymbol{k})\rangle = |\psi_j(\boldsymbol{k})\rangle D_{ji}(\mathcal{PT})$. Under an unitary transformation $U \in \mathrm{U}(2)$, the representation of $D(\mathcal{PT})$ transforms as follows:

$$D'(\mathcal{PT}) = U^{\dagger} D(\mathcal{PT}) U^{*}, \tag{A5}$$

where $|\psi_i'\rangle = |\psi_j\rangle U_{ji}$. Here we want to emphasize that the conjugate operation in Eq. (A5) comes from the antiunitary property [45] of time-reversal operator $\mathcal{T}$. Furthermore, we can divide the U(2) matrix U into SU(2) part and $U(1)$ part as

$$\hat{U} = \mathrm{e}^{i\theta} \exp\left(i \sum_i \frac{\sigma_i}{2} \omega_i \right). \tag{A6}$$

By taking Eq. (A6) into Eq. (A5) and applying anticommutation relation of Pauli matrix, we get

$$D'(\mathcal{PT}) = e^{-2i\theta} D(PT), \tag{A7}$$

which means that the SU(2) part of the unitary transformation do not change the representation of $\mathcal{PT}$. Generally because we want the representation of $\mathcal{PT}$ is independent of $\boldsymbol{k}$, θ should be $\boldsymbol{k}$ independent and ω could be $\boldsymbol{k}$ dependent. Hence that is where the SU(2) gauge [SU(2) Berry connection and SU(2) Berry curvature] comes from.

The Zeeman's coupling $\hat{H}^z(\boldsymbol{k}) = \sum_i d_i(\boldsymbol{k})\sigma_i$ fix the SU(2) gauge $\hat{U}(\boldsymbol{k})$, which diagonalize the Zeeman's coupling

$$\hat{U} = \begin{pmatrix} \cos\frac{\theta_d}{2} & -e^{-i\phi_d}\sin\frac{\theta_d}{2} \\ e^{i\phi_d}\sin\frac{\theta_d}{2} & \cos\frac{\theta_d}{2} \end{pmatrix}, \tag{A8}$$

where

$$\cos\theta_d = \frac{d_z}{|\boldsymbol{d}|} \qquad e^{i\phi_d} = \frac{d_x + i d_y}{\sqrt{d_x^2 + d_y^2}}. \tag{A9}$$

By applying the antiunitary property and representation of $\mathcal{PT}$, we can prove that

$$\begin{aligned} \boldsymbol{A}_1(\boldsymbol{k}) &= i\langle\psi_1(\boldsymbol{k})|\partial_{\boldsymbol{k}}\psi_1(\boldsymbol{k})\rangle = i\langle\mathcal{PT}\partial_{\boldsymbol{k}}\psi_1(\boldsymbol{k})|\mathcal{PT}\psi_1(\boldsymbol{k})\rangle \\ &= i\langle\partial_{\boldsymbol{k}}\mathcal{PT}\psi_1(\boldsymbol{k})|\mathcal{PT}\psi_1(\boldsymbol{k})\rangle = i\langle\partial_{\boldsymbol{k}}\psi_2(\boldsymbol{k})|\psi_2(\boldsymbol{k})\rangle \\ &= -i\langle\psi_2(\boldsymbol{k})|\partial_{\boldsymbol{k}}\psi_2(\boldsymbol{k})\rangle = -\boldsymbol{A}_2(\boldsymbol{k}). \end{aligned}$$

Hence the Berry curvature

$$\begin{aligned} \boldsymbol{F}_1(\boldsymbol{k}) &= \nabla_{\boldsymbol{k}} \times \boldsymbol{A}_1(\boldsymbol{k}) = -\nabla_{\boldsymbol{k}} \times \boldsymbol{A}_2(\boldsymbol{k}) \\ &= -\boldsymbol{F}_2(\boldsymbol{k}). \end{aligned} \tag{A10}$$

By saying the $\boldsymbol{k}\cdot\boldsymbol{p}$ Hamiltonian satisfy the $\mathcal{PT}$ symmetry, we mean $\mathcal{PT}\mathcal{H}(\boldsymbol{k}) = \mathcal{H}(\boldsymbol{k})\mathcal{PT}$, which in matrix form means that

$$D(\mathcal{PT})\hat{H}^*(\boldsymbol{k}) = \hat{H}(\boldsymbol{k})D(\mathcal{PT}). \tag{A11}$$

Similarly the Zeeman's coupling satisfy the $\mathcal{PT}$ symmetry means that

$$D(\mathcal{PT})\hat{\boldsymbol{g}}^*(\boldsymbol{k}) = -\hat{\boldsymbol{g}}(\boldsymbol{k})D(\mathcal{PT}). \tag{A12}$$

Here the minus sign comes from that under $\mathcal{PT}$ operation the magnetic field reverse the direction $\boldsymbol{B} \to -\boldsymbol{B}$.

APPENDIX B: $\boldsymbol{k}\cdot\boldsymbol{p}$ HAMILTONIAN AND 2×2 g-FACTOR TENSOR $\hat{\boldsymbol{g}}(\boldsymbol{k})$ CALCULATIONS

Now we discuss the first-principles calculation of nonmagnetic centrosymmetric semimetals specifically. To balance the accuracy and the efficiency of the calculation we take the two-step down-folding process as introduced below.

As shown in Eq. (6), the $\hat{\boldsymbol{g}}(\boldsymbol{k})$ is inversely proportional to the energy difference $\epsilon_m - \epsilon_l$ between the low-energy subspace and the high-energy subspace. And as shown in Fig. 3(d), for semimetals like $TaAs_2$, the FS contains a number of electron or hole pockets, which are called valleys in this paper. For each valley, we can choose the lowest conduction and highest valence bands as the low-energy subspace (all the rest bands as the high-energy subspace) for the first step and construct the 4×4 $\boldsymbol{k}\cdot\boldsymbol{p}$ model near the valley center $\boldsymbol{K}$. Since within each valley, the average energy distance between the high energy and low energy bands are much bigger than the band dispersion, we can safely approximate the g-factor tensor by a k-independent constant for the 4×4 model.

Here, in particular, we take the representation of the $\mathcal{PT}$ as follows:

$$D(\mathcal{PT}) = \begin{pmatrix} 0 & -i & 0 & 0 \\ i & 0 & 0 & 0 \\ 0 & 0 & 0 & i \\ 0 & 0 & -i & 0 \end{pmatrix}. \tag{B1}$$

TABLE II. Parameters of $\boldsymbol{k}\cdot\boldsymbol{p}$ Hamiltonian for $TaAs_2$.

	Ele-1	Ele-2	Hole-1	Hole-2		Ele-1	Ele-2	Hole-1	Hole-2
$\Omega^{(0)}$	−0.27	−0.15	0.37	0.19	$\Lambda^{(1)}_{2,3}$	0.00	0.00	0.28	−2.03
$\Omega^{(1)}_1$	−0.00	−0.00	−0.00	−0.46	$\Lambda^{(1)}_{3,1}$	0.26	0.78	−0.00	−0.64
$\Omega^{(1)}_2$	−0.74	−0.86	0.00	−0.80	$\Lambda^{(1)}_{3,2}$	−0.00	−0.00	−0.65	−0.75
$\Omega^{(1)}_3$	0.00	−0.00	−0.00	−0.45	$\Lambda^{(1)}_{3,3}$	0.36	−3.33	0.00	−1.02
$\Omega^{(2)}_{11}$	−3.31	3.39	−0.41	−3.52	$\Lambda^{(2)}_{0,11}$	−10.96	−0.62	−0.00	1.81
$\Omega^{(2)}_{12}$, $\Omega^{(2)}_{21}$	0.00	0.00	−0.00	1.55	$\Lambda^{(2)}_{0,12}$, $\Lambda^{(2)}_{0,21}$	0.00	0.00	−0.00	−2.24
$\Omega^{(2)}_{13}$, $\Omega^{(2)}_{31}$	7.21	0.79	1.26	2.67	$\Lambda^{(2)}_{0,13}$, $\Lambda^{(2)}_{0,31}$	1.89	−0.34	0.00	3.08
$\Omega^{(2)}_{22}$	10.45	−4.24	−28.23	−1.67	$\Lambda^{(2)}_{0,22}$	−8.07	2.59	−0.00	−1.55
$\Omega^{(2)}_{23}$, $\Omega^{(2)}_{32}$	0.00	−0.00	0.00	1.20	$\Lambda^{(2)}_{0,23}$, $\Lambda^{(2)}_{0,32}$	0.00	−0.00	−0.00	−0.58
$\Omega^{(2)}_{33}$	4.06	3.56	−0.18	6.32	$\Lambda^{(2)}_{0,33}$	−5.74	−0.06	−0.00	6.01
$\Delta^{(0)}$	−0.07	−0.09	−0.22	−0.10	$\Lambda^{(2)}_{1,11}$	−0.00	−0.00	−0.00	−1.35
$\Delta^{(1)}_1$	−0.00	0.00	−0.00	0.46	$\Lambda^{(2)}_{1,12}$, $\Lambda^{(2)}_{1,21}$	7.81	1.02	−0.00	0.40
$\Delta^{(1)}_2$	−0.74	−0.88	−0.00	0.80	$\Lambda^{(2)}_{1,13}$, $\Lambda^{(2)}_{1,31}$	0.00	0.00	−0.00	−1.31
$\Delta^{(1)}_3$	0.00	−0.00	−0.00	0.45	$\Lambda^{(2)}_{1,22}$	−0.00	−0.00	0.00	−1.69
$\Delta^{(2)}_{11}$	−4.13	0.46	0.56	0.14	$\Lambda^{(2)}_{1,23}$, $\Lambda^{(2)}_{1,32}$	2.33	−0.93	−0.00	−0.44
$\Delta^{(2)}_{12}$, $\Delta^{(2)}_{21}$	0.00	−0.00	−0.00	1.43	$\Lambda^{(2)}_{1,33}$	0.00	−0.00	−0.00	−3.71
$\Delta^{(2)}_{13}$, $\Delta^{(2)}_{31}$	0.30	−0.03	5.10	−0.26	$\Lambda^{(2)}_{2,11}$	−3.67	−1.52	−0.00	−0.08
$\Delta^{(2)}_{22}$	−3.05	0.29	21.01	0.77	$\Lambda^{(2)}_{2,12}$, $\Lambda^{(2)}_{2,21}$	0.00	−0.00	0.00	−2.53
$\Delta^{(2)}_{23}$, $\Delta^{(2)}_{32}$	−0.00	−0.00	0.00	0.42	$\Lambda^{(2)}_{2,13}$, $\Lambda^{(2)}_{2,31}$	1.21	−1.26	0.00	−0.71
$\Delta^{(2)}_{33}$	−2.45	−0.04	−1.22	−2.29	$\Lambda^{(2)}_{2,22}$	−1.23	7.13	−0.00	−2.15
$\Lambda^{(1)}_{0,1}$	−0.00	−0.00	−3.27	−0.44	$\Lambda^{(2)}_{2,23}$, $\Lambda^{(2)}_{2,32}$	0.00	0.00	0.00	−1.85
$\Lambda^{(1)}_{0,2}$	−1.22	0.83	0.00	−1.94	$\Lambda^{(2)}_{2,33}$	0.47	−1.15	−0.00	1.32
$\Lambda^{(1)}_{0,3}$	0.00	−0.00	−0.85	1.88	$\Lambda^{(2)}_{2,11}$	0.00	0.00	−0.00	1.32
$\Lambda^{(1)}_{1,1}$	0.35	−0.49	−0.00	−0.14	$\Lambda^{(2)}_{3,12}$, $\Lambda^{(2)}_{3,21}$	1.32	−1.94	0.00	−1.56
$\Lambda^{(1)}_{1,2}$	0.00	0.00	−0.06	0.28	$\Lambda^{(2)}_{3,13}$, $\Lambda^{(2)}_{3,31}$	−0.00	−0.00	0.00	0.20
$\Lambda^{(1)}_{1,3}$	0.14	2.17	0.00	−0.73	$\Lambda^{(2)}_{3,22}$	−0.00	−0.00	−0.00	−0.70
$\Lambda^{(1)}_{2,1}$	0.00	−0.00	0.03	−0.79	$\Lambda^{(2)}_{3,23}$, $\Lambda^{(2)}_{3,32}$	0.73	1.70	0.00	−1.17
$\Lambda^{(1)}_{2,2}$	0.47	2.81	−0.00	−1.00	$\Lambda^{(2)}_{3,33}$	0.00	0.00	0.00	1.59

By applying Eq. (A11), we find that the Hamiltonian has the following form:

$$\hat{H}(\boldsymbol{k}) = \Omega(\boldsymbol{k}) + \begin{pmatrix} \Delta(\boldsymbol{k}) & \Lambda_\mu(\boldsymbol{k})\sigma_\mu \\ \Lambda_\mu(\boldsymbol{k})\sigma_\mu^\dagger & -\Delta(\boldsymbol{k}) \end{pmatrix}, \tag{B2}$$

where $\Omega(\boldsymbol{k})$, $\Delta(\boldsymbol{k})$, and $\Lambda_\mu(\boldsymbol{k})$ are real functions of $\boldsymbol{k}$, $\mu = 0, 1, 2, 3$, and σ_μ are Pauli matrices except σ_0

$$\sigma_0 = i\begin{pmatrix} 1 & 0 \\ 0 & 1 \end{pmatrix}. \tag{B3}$$

And for $f = \Omega, \Delta, \Lambda_\mu$ the $\boldsymbol{k}$ dependence has the following form:

$$f(\boldsymbol{k}) = f^{(0)} + \sum_i f_i^{(1)} k_i + \sum_{ij} f_{ij}^{(2)} k_i k_j. \tag{B4}$$

The corresponding 4×4 g-factor matrix has the following form (here we have included the spin contribution in the low-energy subspace and orbital contribution from the high-energy subspace):

$$\hat{\boldsymbol{g}}^{(4)} = \begin{pmatrix} \boldsymbol{g}^a & \boldsymbol{g}^b + i\boldsymbol{g}^c & \boldsymbol{g}^e + i\boldsymbol{g}^f & \boldsymbol{g}^g + i\boldsymbol{g}^h \\ \boldsymbol{g}^b - i\boldsymbol{g}^c & -\boldsymbol{g}^a & -\boldsymbol{g}^g + i\boldsymbol{g}^h & \boldsymbol{g}^e - i\boldsymbol{g}^f \\ \boldsymbol{g}^e - i\boldsymbol{g}^f & -\boldsymbol{g}^g - i\boldsymbol{g}^h & \boldsymbol{g}^l & \boldsymbol{g}^m + i\boldsymbol{g}^n \\ \boldsymbol{g}^g - i\boldsymbol{g}^h & \boldsymbol{g}^e + i\boldsymbol{g}^f & \boldsymbol{g}^m - i\boldsymbol{g}^n & -\boldsymbol{g}^l \end{pmatrix}. \tag{B5}$$

The corresponding parameters for $ZrTe_5$ are summarized in Ref. [3] and parameters for $TaAs_2$ are summarized in Table II and Table III. All these parameters are obtained by first-principles calculation introduced in the main text and Ref. [3].

The eigenvalue of $\boldsymbol{k}\cdot\boldsymbol{p}$ Hamiltonian is

$$\epsilon^{\pm}(\boldsymbol{k}) = \Omega(\boldsymbol{k}) \pm \sqrt{\Delta(\boldsymbol{k})^2 + \sum_\mu \Lambda_\mu(\boldsymbol{k})^2}. \tag{B6}$$

And the unitary transformation, which can diagonalize the $\boldsymbol{k}\cdot\boldsymbol{p}$ Hamiltonian is

TABLE III. Parameters of 4×4 g factor for $TaAs_2$.

	Ele-1	Ele-2	Hole-1	Hole-2		Ele-1	Ele-2	Hole-1	Hole-2
g_1^a	−0.71	−0.28	−0.60	0.28	g_1^g	0.00	−0.00	−0.00	0.10
g_2^a	−0.00	0.00	−0.00	−0.08	g_2^g	−1.50	−0.24	0.00	−0.41
g_3^a	−0.64	0.44	−0.88	0.12	g_3^g	0.00	−0.00	−0.00	−0.44
g_1^b	0.06	−0.07	0.46	0.03	g_1^h	0.42	−0.17	−0.00	0.06
g_2^b	0.00	−0.00	0.00	0.12	g_2^h	−0.00	0.00	−0.00	−0.74
g_3^b	−1.63	0.45	−0.63	−0.44	g_3^h	0.70	−0.93	−0.00	0.63
g_1^c	0.00	0.00	−0.00	−0.93	g_1^l	0.25	0.64	0.21	0.44
g_2^c	−0.25	−0.17	0.97	0.76	g_2^l	0.00	−0.00	−0.00	0.78
g_3^c	0.00	−0.00	0.00	0.70	g_3^l	−0.59	−0.15	−2.06	0.93
g_1^e	0.00	0.00	0.00	−0.02	g_1^m	−0.54	1.82	0.72	−0.05
g_2^e	0.04	−0.92	−0.00	−0.17	g_2^m	−0.00	0.00	0.00	−0.10
g_3^e	0.00	0.00	0.00	−0.39	g_3^m	−1.37	0.42	−1.43	0.03
g_1^f	−0.81	0.18	−0.00	−0.07	g_1^n	−0.00	0.00	−0.00	−0.41
g_2^f	−0.00	0.00	0.00	0.53	g_2^n	−0.75	0.17	0.91	−0.86
g_3^f	0.08	−0.45	−0.00	0.60	g_3^n	−0.00	−0.00	−0.00	−0.30

$$\hat{V}(\boldsymbol{k}) = \begin{pmatrix} \sqrt{\frac{\epsilon^- - \Omega + \Delta}{2(\epsilon^- - \Omega)}} \begin{pmatrix} \begin{pmatrix} 1 & 0 \\ 0 & 1 \end{pmatrix} \\ \frac{1}{\epsilon^- - \Omega + \Delta} \begin{pmatrix} \Lambda_3 - \mathrm{i}\Lambda_0 & \Lambda_1 - \mathrm{i}\Lambda_2 \\ \Lambda_1 + \mathrm{i}\Lambda_2 & -\Lambda_3 - \mathrm{i}\Lambda_0 \end{pmatrix} \end{pmatrix} \sqrt{\frac{\epsilon^+ - \Omega - \Delta}{2(\epsilon^+ - \Omega)}} \begin{pmatrix} \frac{1}{\epsilon^+ - \Omega - \Delta} \begin{pmatrix} \Lambda_3 + \mathrm{i}\Lambda_0 & \Lambda_1 - \mathrm{i}\Lambda_2 \\ \Lambda_1 + \mathrm{i}\Lambda_2 & -\Lambda_3 + \mathrm{i}\Lambda_0 \end{pmatrix} \\ \begin{pmatrix} 1 & 0 \\ 0 & 1 \end{pmatrix} \end{pmatrix} \end{pmatrix}. \tag{B7}$$

Now we take the second down-folding process. Around any wave vector $\boldsymbol{k}$, the $\boldsymbol{k} \cdot \boldsymbol{p}$ Hamiltonian in linear approximation transformed by the unitary transformation $\hat{V}(\boldsymbol{k})$ at $\boldsymbol{k}$ has the following form:

$$\tilde{H}_{mm'}(\boldsymbol{k} + \Delta\boldsymbol{k}) = \hat{V}(\boldsymbol{k})^\dagger H(\boldsymbol{k} + \Delta\boldsymbol{k}) \hat{V}(\boldsymbol{k}) \tag{B8}$$

$$= \epsilon_m(\boldsymbol{k}) \delta_{mm'} + \tilde{\boldsymbol{v}}_{mm'}(\boldsymbol{k}) \cdot \Delta\boldsymbol{k}, \tag{B9}$$

where $\tilde{v}(\boldsymbol{k}) = \hat{V}^\dagger(\boldsymbol{k}) \frac{\partial \hat{H}(\boldsymbol{k})}{\partial \boldsymbol{k}} \hat{V}(\boldsymbol{k})$, $\epsilon_{1,2} = \epsilon_-$(named holelike bands), $\epsilon_{3,4} = \epsilon_+$(named electronlike bands). Then the g factor for holelike (electronlike) bands contributed by the electronlike (holelike) bands can be calculated with Eq. (6) as follows, which is $\boldsymbol{k}$ dependent

$$\hat{\boldsymbol{g}}^{(2)}_{pp'}(\boldsymbol{k}) = \frac{i m_\mathrm{e}}{\hbar^2} \frac{\chi}{\epsilon^+ - \epsilon^-} \sum_{q,ijk} \tilde{v}_{pq,i}(\boldsymbol{k}) \tilde{v}_{qp',j}(\boldsymbol{k}) \varepsilon_{ijk} \boldsymbol{e}_k, \tag{B10}$$

where, for electronlike bands, $\chi = -1$, $p, p' = 3, 4$, and $q = 1, 2$; for holelike bands, $\chi = 1$, $p, p' = 1, 2$, and $q = 3, 4$. Hence the total g factor is

$$\hat{\boldsymbol{g}}_{pp'}(\boldsymbol{k}) = \hat{\boldsymbol{g}}^{(2)}_{pp'}(\boldsymbol{k}) + \sum_{mm'} \hat{V}^\dagger_{pm}(\boldsymbol{k}) \hat{\boldsymbol{g}}^{(4)}_{mm'} V_{m'p'}(\boldsymbol{k}). \tag{B11}$$

APPENDIX C: DERIVATIONS FOR EQ. (7), EQ. (8), AND EQ. (12)

Accroding to Lifshitz-Kosevich formula, the quantum oscillation contributed by one FS is $\Delta\rho(B) \propto \cos(\hbar S_\mathrm{ex}/eB + \gamma + \phi)$, where S_ex is the area of the extreme cross section of the FS, which is perpendicular to the magnetic field as shown in Fig. 7.

For centrosymmetric semimetals such as $ZrTe_5$, under magnetic field the Zeeman effect splits the otherwise degenerate FS and induces extra Berry phases. Hence, the quantum oscillation is

$$\Delta\rho(B) \propto \cos\left(\frac{\hbar(S^0_\mathrm{ex} + \Delta S_\mathrm{ex})}{eB} + \gamma + \phi\right) + \cos\left(\frac{\hbar(S^0_\mathrm{ex} - \Delta S_\mathrm{ex})}{eB} + \gamma - \phi\right). \tag{C1}$$

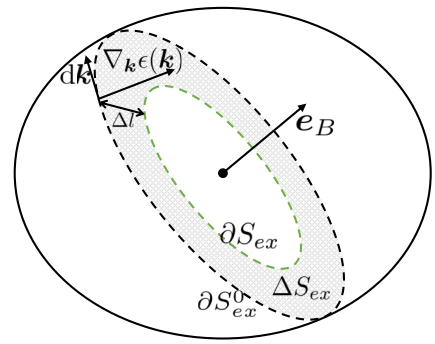

FIG. 7. Schematic diagram for the Zeeman splitting of FS's extreme cross section. The boundary of FS's extreme cross section ∂S^0_ex (∂S_ex) without (with) magnetic field is indicated in black (blue) dotted line. For concision only the shrunk one of the split extreme cross sections is plotted.

Here the $S_{\rm ex}^0$ is the extreme cross-section area without magnetic field. By applying sum-to-product identity, we have

$$\Delta\rho(B) \propto \cos\left(\frac{\hbar S_{\rm ex}^0}{eB} + \gamma\right)\cos\left(\frac{\hbar \Delta S_{\rm ex}}{eB} + \phi\right). \tag{C2}$$

Because the change of the FS induced by Zeeman effect is small for magnetic field strength that can be achieved in experiments, $\Delta S_{\rm ex}$ can be expressed as a line integral of splitting width Δl along the boundary of $S_{\rm ex}^0$ as shown in Fig. 7

$$\Delta S_{\rm ex} = \oint_{\partial S_{\rm ex}^0} \Delta l\, dk. \tag{C3}$$

And the splitting width Δl can be expressed as splitting energy $\sqrt{\det|\mu_B \hat{\boldsymbol{g}}(\boldsymbol{k})\cdot\boldsymbol{B}|}$ divided by the projection of energy gradient $|\nabla_{\boldsymbol{k}}\epsilon(\boldsymbol{k})\cdot(\frac{d\boldsymbol{k}}{dk}\times\boldsymbol{e}_B)|$ (because generally the energy gradient $\nabla_{\boldsymbol{k}}\epsilon(\boldsymbol{k})$ is not in the plane of extreme cross section). The projection of energy gradient can be simplified as

$$\begin{aligned}\left|\nabla_{\boldsymbol{k}}\epsilon(\boldsymbol{k})\cdot\left(\frac{d\boldsymbol{k}}{dk}\times\boldsymbol{e}_B\right)\right| &= \left|\frac{d\boldsymbol{k}}{dk}\cdot(\nabla_{\boldsymbol{k}}\epsilon(\boldsymbol{k})\times\boldsymbol{e}_B)\right| \\ &= |\nabla_{\boldsymbol{k}}\epsilon(\boldsymbol{k})\times\boldsymbol{e}_B|. \end{aligned}\tag{C4}$$

Hence the splitting width is

$$\Delta l = \frac{\sqrt{\det|\mu_B \hat{\boldsymbol{g}}(\boldsymbol{k})\cdot\boldsymbol{B}|}}{|\nabla_{\boldsymbol{k}}\epsilon(\boldsymbol{k})\times\boldsymbol{e}_B|}. \tag{C5}$$

With combing Eq. (C2), Eq. (C3), and Eq. (C5) and taking $\alpha = \Delta S_{\rm ex}/B$, we get Eq. (7) and Eq. (8). And for electron (hole) pocket, the sign χ is defined as -1 $(+1)$, because under Zeeman effect the FS with positive Zeeman splitting energy will shrink (expand).

Now the derivation of Eq. (12) is straightforward. As stated in the main text, with the presence of magnetic field, the Zeeman effect will split these states and the net contribution to the AHC comes from a thin shell near the FS where only one of these otherwise degenerate states is occupied. Hence the AHC is a surface integral for the product of Berry curvature F_+^k and the splitting width Δd

$$\sigma_{ij} = -\varepsilon_{ijk}\frac{e^2}{\hbar}\sum_n \int_{FS} 2\,\Delta d\, F_+^k(\boldsymbol{k})\, dS. \tag{C6}$$

Similarly the splitting energy width Δd can be expressed as splitting energy $\sqrt{\det|\mu_B \hat{\boldsymbol{g}}(\boldsymbol{k})\cdot\boldsymbol{B}|}$ divided by energy gradient $|\nabla_{\boldsymbol{k}}\epsilon(\boldsymbol{k})|$ (no projection)

$$\Delta d = \frac{\sqrt{\det|\mu_B \hat{\boldsymbol{g}}(\boldsymbol{k})\cdot\boldsymbol{B}|}}{|\nabla_{\boldsymbol{k}}\epsilon(\boldsymbol{k})|}. \tag{C7}$$

By combining $\sigma_{ij} = \lambda_{ij,k}B_k$ and Bohr magnetic $\mu_B = \frac{e\hbar}{2m_e}$, Eq. (C6) and Eq. (C7), we get Eq. (12).

[1] M. H. Cohen and E. I. Blount, The g-factor and de haas-van alphen effect of electrons in bismuth, Philos. Mag. **5**, 115 (1960).

[2] J. M. Luttinger and W. Kohn, Motion of electrons and holes in perturbed periodic fields, Phys. Rev. **97**, 869 (1955).

[3] Z.-D. Song, S. Sun, Y.-F. Xu, S.-M. Nie, H.-M. Weng, Z. Fang, and X. Dai, First principle calculation of the effective zeeman's couplings in topological materials, arXiv:1512.05084 [cond-mat.mtrl-sci].

[4] G. P. Mikitik and Y. V. Sharlai, Manifestation of Berry's Phase in Metal Physics, Phys. Rev. Lett. **82**, 2147 (1999).

[5] Y. Zhang, Y.-W. Tan, H. L. Stormer, and P. Kim, Experimental observation of the quantum hall effect and berry's phase in graphene, Nature (London) **438**, 201 (2005).

[6] K. S. Novoselov, E. McCann, S. V. Morozov, V. I. Fal'ko, M. I. Katsnelson, U. Zeitler, D. Jiang, F. Schedin, and A. K. Geim, Unconventional quantum hall effect and berry's phase of 2p in bilayer graphene, Nature Phys. **2**, 177 (2006).

[7] D. Shoenberg, *Magnetic Oscillations in Metals*, Cambridge Monographs on Physics (Cambridge University Press, Cambridge, 1984), pp. 1–41, 448.

[8] N. Nagaosa, J. Sinova, S. Onoda, A. H. MacDonald, and N. P. Ong, Anomalous Hall effect, Rev. Mod. Phys. **82**, 1539 (2010).

[9] Z. Fang, N. Nagaosa, K. S. Takahashi, A. Asamitsu, R. Mathieu, T. Ogasawara, H. Yamada, M. Kawasaki, Y. Tokura, and K. Terakura, The anomalous Hall effect and magnetic monopoles in momentum space, Science **302**, 92 (2003).

[10] T. Jungwirth, Q. Niu, and A. H. MacDonald, Anomalous Hall Effect in Ferromagnetic Semiconductors, Phys. Rev. Lett. **88**, 207208 (2002).

[11] X. Wan, A. M. Turner, A. Vishwanath, and S. Y. Savrasov, Topological semimetal and fermi-arc surface states in the electronic structure of pyrochlore iridates, Phys. Rev. B **83**, 205101 (2011).

[12] A. A. Soluyanov, D. Gresch, Z. Wang, Q. Wu, M. Troyer, X. Dai, and B. A. Bernevig, Type-ii Weyl semimetals, Nature (London) **527**, 495 (2015).

[13] Z. Wang, Y. Sun, X.-Q. Chen, C. Franchini, G. Xu, H. Weng, X. Dai, and Z. Fang, Dirac semimetal and topological phase transitions in A_3bi (a = Na, k, rb), Phys. Rev. B **85**, 195320 (2012).

[14] Z. K. Liu, J. Jiang, B. Zhou, Z. J. Wang, Y. Zhang, H. M. Weng, D. Prabhakaran, S.-K. Mo, H. Peng, P. Dudin, T. Kim, M. Hoesch, Z. Fang, X. Dai, Z. X. Shen, D. L. Feng, Z. Hussain, and Y. L. Chen, A stable three-dimensional topological dirac semimetal Cd_3As_2, Nature Mater. **13**, 677 (2014).

[15] H. Weng, C. Fang, Z. Fang, B. A. Bernevig, and X. Dai, Weyl Semimetal Phase in Noncentrosymmetric Transition-Metal Monophosphides, Phys. Rev. X **5**, 011029 (2015).

[16] B. Q. Lv, H. M. Weng, B. B. Fu, X. P. Wang, H. Miao, J. Ma, P. Richard, X. C. Huang, L. X. Zhao, G. F. Chen, Z. Fang, X. Dai, T. Qian, and H. Ding, Experimental Discovery of Weyl Semimetal Taas, Phys. Rev. X **5**, 031013 (2015).

[17] S.-Y. Xu, I. Belopolski, N. Alidoust, M. Neupane, G. Bian, C. Zhang, R. Sankar, G. Chang, Z. Yuan, C.-C. Lee, S.-M. Huang, H. Zheng, J. Ma, D. S. Sanchez, B. Wang, A. Bansil, F. Chou, P. P. Shibayev, H. Lin, S. Jia, and M. Z. Hasan, Discovery of a Weyl fermion semimetal and topological fermi arcs, Science **349**, 613 (2015).

[18] Y. Kim, B. J. Wieder, C. L. Kane, and A. M. Rappe, Dirac Line Nodes in Inversion-Symmetric Crystals, Phys. Rev. Lett. **115**, 036806 (2015).

[19] L. M. Schoop, M. N. Ali, C. Straßer, A. Topp, A. Varykhalov, D. Marchenko, V. Duppel, S. S. P. Parkin, B. V. Lotsch, and C. R. Ast, Dirac cone protected by non-symmorphic symmetry and three-dimensional dirac line node in ZrSiS, Nature Commun. **7**, 11696 (2016).

[20] N. P. Armitage, E. J. Mele, and A. Vishwanath, Weyl and dirac semimetals in three-dimensional solids, Rev. Mod. Phys. **90**, 015001 (2018).

[21] K. Fukushima, D. E. Kharzeev, and H. J. Warringa, Chiral magnetic effect, Phys. Rev. D **78**, 074033 (2008).

[22] Q. Li, D. E. Kharzeev, C. Zhang, Y. Huang, I. Pletikosic, A. V. Fedorov, R. D. Zhong, J. A. Schneeloch, G. D. Gu, and T. Valla, Chiral magnetic effect in $ZrTe_5$, Nature Phys. **12**, 550 (2016).

[23] D. T. Son and N. Yamamoto, Berry Curvature, Triangle Anomalies, and the Chiral Magnetic Effect in Fermi Liquids, Phys. Rev. Lett. **109**, 181602 (2012).

[24] H. B. Nielsen and M. Ninomiya, The Adler-Bell-Jackiw anomaly and Weyl fermions in a crystal, Phys. Lett. B **130**, 389 (1983).

[25] X. Huang, L. Zhao, Y. Long, P. Wang, D. Chen, Z. Yang, H. Liang, M. Xue, H. Weng, Z. Fang, X. Dai, and G. Chen, Observation of the Chiral-Anomaly-Induced Negative Magnetoresistance in 3d Weyl Semimetal Taas, Phys. Rev. X **5**, 031023 (2015).

[26] D. T. Son and B. Z. Spivak, Chiral anomaly and classical negative magnetoresistance of Weyl metals, Phys. Rev. B **88**, 104412 (2013).

[27] A. Sekine and K. Nomura, Electron correlation induced spontaneous symmetry breaking and Weyl semimetal phase in a strongly spin-orbit coupled system, J. Phys. Soc. Jpn. **82**, 033702 (2013).

[28] D. Xiao, M.-C. Chang, and Q. Niu, Berry phase effects on electronic properties, Rev. Mod. Phys. **82**, 1959 (2010).

[29] R. Winkler, *Spin-Orbit Coupling Effects in Two-Dimensional Electron and Hole Systems*, Springer Tracts in Modern Physics, Vol. 191 (Springer, Berlin, 2003), pp. 9–11, 201–205.

[30] P.-O. Löwdin, A note on the quantum-mechanical perturbation theory, J. Chem. Phys. **19**, 1396 (1951).

[31] N. Ashcroft and N. Mermin, *Solid State Physics*, HRW international editions (Holt, Rinehart and Winston, New York, 1976), pp. 263–282.

[32] H. Weng, X. Dai, and Z. Fang, Transition-Metal Pentatelluride $ZrTe_5$ and $HfTe_5$: A Paradigm for Large-Gap Quantum Spin Hall Insulators, Phys. Rev. X **4**, 011002 (2014).

[33] Y. Liu, X. Yuan, C. Zhang, Z. Jin, A. Narayan, C. Luo, Z. Chen, L. Yang, J. Zou, X. Wu, S. Sanvito, Z. Xia, L. Li, Z. Wang, and F. Xiu, Zeeman splitting and dynamical mass generation in dirac semimetal $ZrTe_5$, Nature Commun. **7**, 12516 (2016).

[34] G. Zheng, J. Lu, X. Zhu, W. Ning, Y. Han, H. Zhang, J. Zhang, C. Xi, J. Yang, H. Du, K. Yang, Y. Zhang, and M. Tian, Transport evidence for the three-dimensional dirac semimetal phase in $ZrTe_5$, Phys. Rev. B **93**, 115414 (2016).

[35] G. N. Kamm, D. J. Gillespie, A. C. Ehrlich, T. J. Wieting, and F. Levy, Fermi surface, effective masses, and dingle temperatures of $ZrTe_5$ as derived from the Shubnikov–de Haas effect, Phys. Rev. B **31**, 7617 (1985).

[36] J. Wang, J. Niu, B. Yan, X. Li, R. Bi, Y. Yao, D. Yu, and X. Wu, Vanishing quantum oscillations in dirac semimetal $ZrTe_5$, Proc. Natl. Acad. Sci. USA **115**, 9145 (2018).

[37] Y. X. Zhao, A. P. Schnyder, and Z. D. Wang, Unified Theory of *pt* and *cp* Invariant Topological Metals and Nodal Superconductors, Phys. Rev. Lett. **116**, 156402 (2016).

[38] A. A. Burkov, Chiral Anomaly and Diffusive Magnetotransport in Weyl Metals, Phys. Rev. Lett. **113**, 247203 (2014).

[39] A. A. Burkov, Negative longitudinal magnetoresistance in Dirac and Weyl metals, Phys. Rev. B **91**, 245157 (2015).

[40] J. Xiong, S. K. Kushwaha, T. Liang, J. W. Krizan, M. Hirschberger, W. Wang, R. J. Cava, and N. P. Ong, Evidence for the chiral anomaly in the Dirac semimetal Na3bi, Science **350**, 413 (2015).

[41] X. Wang, J. R. Yates, I. Souza, and D. Vanderbilt, *Ab initio* calculation of the anomalous Hall conductivity by Wannier interpolation, Phys. Rev. B **74**, 195118 (2006).

[42] K. Persson, Materials data on taas2 (sg:12) by materials project, 2015, an optional note.

[43] Y. Luo, R. D. McDonald, P. F. S. Rosa, B. Scott, N. Wakeham, N. J. Ghimire, E. D. Bauer, J. D. Thompson, and F. Ronning, Anomalous electronic structure and magnetoresistance in $TaAs_2$, Sci. Rep. **6**, 27294 (2016).

[44] Z. Yuan, H. Lu, Y. Liu, J. Wang, and S. Jia, Large magnetoresistance in compensated semimetals $TaAs_2$ and $NbAs_2$, Phys. Rev. B **93**, 184405 (2016).

[45] J. J. Sakurai, *Modern Quantum Mechanics* (Addison-Wesley, Boston, 1994), p. 269.